**Article:**

# On the monolithic and staggered solution of cell contractility and focal adhesion growth

Pradeep Keshavanarayana[*1], Martin Ruess[1], René de Borst[2]

[1] *School of Engineering, University of Glasgow, UK*
[2] *Department of Civil and Structural Engineering, University of Sheffield, UK*

## SUMMARY

The mechanical response of cells to stimuli tightly couples bio-chemical and bio-mechanical processes which describe fundamental properties such as cell growth and re-orientation. Cells interact continuously with their external surroundings, the extra cellular matrix (ECM), by establishing a bond between cell and ECM through the formation of focal adhesions. Focal adhesions are made up of integrins which are mechanosensitive proteins and responsible for the communication between the cell and the ECM. The governing bio-chemo-mechanical processes can be modeled by means of a continuum approach considering mechanical and thermodynamic equilibrium to describe cell contractility and focal adhesion growth. The immanent multi-physical character of cell mechanics involves important aspects such as the coupling of fields of different scales and corresponding interface conditions which are sensitive to the solution of the governing numerical problem. These aspects become even more relevant when considering a feedback loop among the multi-physical solutions fields.

In this contribution, we consider solution properties and sensitivity aspects of a non-linear mechanical continuum model for the prognosis of stress fiber growth and re-orientation incorporating a mechanosensitive feedback loop. We provide the governing equations of a Hill-model based stress fiber growth which is coupled to a thermodynamical approach modeling the focal adhesions. Furthermore, a variational formulation including the algebraic equations is derived for staggered and monolithic solution approaches, and the reaction-diffusion equation which models the feedback mechanism. We test both schemes with regard to reliability, accuracy and numerical efficiency for different model parameters and loading scenarios. We present algorithmic aspects of the considered solution schemes and reveal their robustness with regard to model refinement in space and time, and finally provide an assessment of their overall solution performance for multi-physics problems in the context of cell mechanics.
Copyright © 2018 John Wiley & Sons, Ltd.

*Correspondence to: p.keshavanarayana.1@research.gla.ac.uk

*Prepared using cnmauth.cls [Version: 2010/03/27 v2.00]*

## 1. INTRODUCTION

The process of growth and reproduction in biological life cycles is tightly connected with the bio-chemical and mechanical properties of cells and their response behavior. Cells are the basic units of living organisms which constantly transfer and exchange material and information with their surroundings. Some of the fundamental mechanisms of these processes have been understood fairly well by numerous *in-vitro* experiments revealing e.g. the dependencies between cell stiffness and cell proliferation under changing loading conditions [1, 2, 3, 4], or the ability of cells to respond to external mechanical cues [5, 6]. In addition to biological experiments, mathematical models have been developed to bolster *in-vitro* experiments, to allow for a prediction of *in-vivo* behaviour of cells [7, 8, 9, 10, 11] and to support the identification of essential cell properties.

The immanent multi-physics nature of these models requires the consideration and coupling of bio-chemical and mechanical phenomena described by a set of partial differential equations of different nature with implications for the numerical solution process. In particular, from the field of fluid-structure interaction a number of well-documented research studies exists [12, 13] which address carefully the numerical aspects and properties of different multi-physical solution procedures, including bio-medical applications [14, 15]. Surprisingly, little attention has been paid to solution aspects and properties in the field of cell mechanics revealing the robustness, reliability and accuracy of the governing coupled problem. Only a few papers report about the solution scheme which generally follows a staggered approach with partially fixed solution fields in every time step [9]. For small time steps these schemes ensure a sufficient level of robustness and accuracy, but may fail for larger time steps which can be necessary to efficiently cover the large time scale of calcium growth which affects the mechanical equilibrium.

In this article, we extend a recently introduced model describing cell contractility and corresponding focal adhesion growth [16], to a geometrically non-linear formulation in order to account for large displacement effects as commonly observed in *in-vitro* experiments. Moreover, we carefully study different solution methods for the bio-chemo-mechanical equations to reveal essential solution properties with regard to robustness and accuracy. The solution methods that we have considered, staggered and monolithic, follow different ways of coupling the governing equations. Such solution methods along with a consistent large displacement analysis are universal for a large class of coupled problems in general [15] and bio-mechanical problems in particular [17]. To this end, we provide a consistent variational formulation and the corresponding algebraic equations tailored to the different solution methods. The basic differences of the solution schemes are considered in terms of algorithmic aspects and are illustrated with a number of numerical experiments, including model refinement in space and time. Furthermore, we study the sensitivity of the solution with regard to parameter variations representing different model properties and apply cyclic loading to understand the mechanisms of the stress fiber generation.

The structure of the manuscript is as follows. In section 2, we briefly introduce the bio-chemo-mechanical model to provide the set of equations which governs the cell contractility, the related stress fiber growth and the feedback loop. More importantly, we provide a concise summary of the essential solution strategies considered in this contribution, namely the staggered and monolithic solution approaches. In section 3, we present in compact form the basic terminology of a geometrically non-linear continuum formulation as used in the contractility model. We derive the governing variational equations and corresponding discrete equations for the staggered and monolithic solution approaches. Algorithmic aspects of the two methods are presented and discussed in section 4 and implemented and tested with a number of numerical tests, presented in section 5. We summarize and conclude the main findings in section 6.

## 2. BIO-CHEMO-MECHANICAL CELL MODEL

We start with a brief summary of the coupled bio-chemo-mechanical model which relates cell contractility and focal adhesion growth considering a feedback loop. The model was discussed in detail in [16]. It is included here for completeness, and we limit ourselves to the formulation of the

model's key constituents. We introduce the terminology used for the extension to a large displacement formulation and consider different solution schemes for the coupled equations.

### 2.1. Coupled 'cell contractility - focal adhesion growth' model

The model essentially comprises of two governing equations, representing the mechanical equilibrium in terms of a force equilibrium of the cell, and focal adhesion growth connecting cell and extra-cellular matrix (ECM). In addition, a calcium growth model is considered which connects the focal adhesion formation to the current stress fiber concentration in the cell through cytoplasmic calcium and so establishes a feedback loop [16]. In the following, we assume the model behaviour to represent a state of plane stress.

*2.1.1. Mechanical equilibrium* Consideration of the balance equations provides the mechanical equilibrium including total stress in the cell $S_{ij}$ and the external force $T_i$ which is exerted by the focal adhesion on the cell

$$b\, S_{ij,j} \quad = \quad T_i \qquad\qquad i,j = 1,2 \tag{1}$$

where $b$ is the cell thickness. The total stress is split additively into an *active* stress and a *passive* stress contribution, $S_{ij}^a$ and $S_{ij}^p$, respectively. The active stress originates from the contracting actin filaments in the cell's cytoskeleton whereas the passive stress results from the resistance offered by the cytoplasm. The mechanical equilibrium, eq. (1), represents a 2-dimensional homogenization of the anisotropic stress fiber contraction in the state-of-plane-stress cell model. The underlying growth model, briefly summarized in the following, is formulated in terms of a directional stress fiber concentration.

*Active stress*  The active stress is characterized by effects of the strain $\varepsilon$ and the strain rate $\dot{\varepsilon}$, as

$$\kappa \quad := \quad \frac{\sigma^a(\phi)}{\sigma_0(\phi)} \quad = \quad f(\varepsilon)\, g(\dot{\varepsilon}) \tag{2}$$

$$\sigma_0(\phi) \quad = \quad \eta(\phi)\, \sigma_{max} \tag{3}$$

where $\sigma^a(\phi)$ is the directional *active* stress and $\sigma_0(\phi)$ is the isometric stress expressed in terms of the maximum allowed stress $\sigma_{max}$ and a fiber angle $\phi$ dependent stress fiber concentration $(0 \leq \eta(\phi) \leq 1)$. The growth model follows from the corresponding concentration rate:

$$\dot{\eta}(\phi) \quad = \quad \begin{cases} (1 - \eta(\phi))\, C\, k_f - (1 - \kappa)\, \eta(\phi)\, k_b & \text{if } \kappa < 1 \\[2mm] (1 - \eta(\phi))\, C\, k_f & \text{if } \kappa \geq 1 \end{cases} \tag{4}$$

with $k_f$ and $k_b$ being rate constants related to the association and dissociation of stress fibers, respectively and $C$ represents the cytoplasmic calcium concentration. For details about the growth model and its influence on the equilibrium equations, we refer to KESHAVANARAYANA ET AL. [16]. The growth of active stress is assumed to follow a Hill type growth [18] depending on the strain rate

$$g(\dot{\varepsilon}) \quad = \quad \frac{1}{1 + \frac{S_{\text{exp}}}{\sqrt{(S_{\text{exp}}^2 + 1)}}} \left( 1 + \frac{\bar{k}_v \frac{\dot{\varepsilon}}{\dot{\varepsilon}_0} + S_{\text{exp}}}{\sqrt{\left( \bar{k}_v \frac{\dot{\varepsilon}}{\dot{\varepsilon}_0} + S_{\text{exp}} \right)^2 + 1}} \right) \tag{5}$$

where, $\bar{k}_v$ is the Hill constant, $\dot{\varepsilon}_0$ is the strain rate sensitivity, $\dot{\varepsilon}$ is the strain rate and $S_{\text{exp}}$ is an expansion parameter with significance for cyclic cell loading only. For cyclic loading we use $S_{\text{exp}} = 1$, else $S_{\text{exp}} = 0$.

The stress-strain relation is expressed in analogy to the characteristics of cables which are stiff in tension but which have no stiffness in compression

$$
f(\varepsilon) = \begin{cases} \exp\left(-\left(\frac{\varepsilon}{\varepsilon_0}\right)^2\right) & \text{if } \varepsilon < 0 \\ \exp\left(-\left(\frac{\varepsilon}{\varepsilon_0}\right)^2\right) + \left(\frac{\varepsilon}{\varepsilon_1}\right)^2 & \text{if } \varepsilon \geq 0. \end{cases} \tag{6}
$$

in which $\varepsilon$ is the strain, $\varepsilon_0$ and $\varepsilon_1$ are constants characterizing the decay of contraction of the cell and passive strain hardening, respectively [16, 10].

*Passive stress* The passive stress is assumed to follow a linear elastic behavior

$$
\sigma^P = E\,\varepsilon \tag{7}
$$

where $\varepsilon$ is the axial fiber strain and $E$ is the Young's modulus of the cell.

*2.1.2. Thermodynamic equilibrium* For cells to adhere to the ECM, focal adhesions have to form a bond with the cell membrane. In this regard, proteins forming focal adhesions can be assumed to be made up of low affinity integrins $\mu_L$ and high affinity integrins $\mu_H$, where integrins are mechanically sensitive proteins. As shown in Figure 1, low affinity integrins do not form a bond between the cell and the ECM, while high affinity integrins do form a bond. It is assumed that these integrins satisfy thermodynamic equilibrium, thereby resulting in the mutual conversion of integrins when necessary.
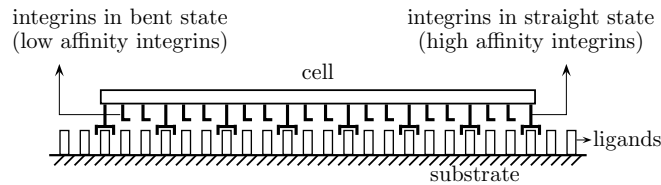


Figure 1. Low and high affinity integrins.

The chemical potential of low and high affinity integrins is

$$
\mu_L = \mu_L^R + kT\,\ln\left(\frac{\xi_L}{\xi_0}\right) \tag{8}
$$

$$
\mu_H = \mu_H^R + kT\,\ln\left(\frac{\xi_H}{\xi_0}\right) + \Phi - \bar{F}\,\Delta \tag{9}
$$

where $\mu_L$ and $\mu_H$ are the chemical potentials of the low and high affinity integrins, respectively. Furthermore, $\mu_L^R$ and $\mu_H^R$ are the reference chemical potentials while $\xi_L$ and $\xi_H$ are the concentrations of the low and high affinity integrins, respectively. The Boltzmann constant is denoted by $k$ and the absolute temperature by $T$. Furthermore, $\xi_0$ denotes the reference number of integrins [19]. The contribution $(\bar{F}\,\Delta)$ represents the work done by the bond while being stretched by $\Delta$. The bond energy is denoted by $\Phi$ and is assumed to depend quadratically on the stretch [16]. Finally, the requirement of thermodynamic equilibrium results in the identity

$$
\mu_H = \mu_L \tag{10}
$$

which leads to the ratio $\alpha$ of the integrin concentration

$$
\alpha := \frac{\xi_H}{\xi_L} = \exp\left(\frac{\mu_L^R - \mu_H^R - \Phi + \bar{F}\,\Delta}{kT}\right) \tag{11}
$$

with the total number of integrins being conserved at

$$\xi_0 \;\; = \;\; \xi_H + \xi_L \,. \tag{12}$$

The conservation of integrins allows the conversion between low and high affinity integrins based on their potential expressed as

$$\xi_H \;\; = \;\; \frac{\xi_0 \, \alpha}{1 + \alpha} \,. \tag{13}$$

Thus, high affinity integrins exert a force on the cell, which depends on the stretch $\Delta$ experienced by the bond and the bond stiffness, $\lambda_s$:

$$\bar{T} \;\; = \;\; \xi_H \, \bar{F} \;\; = \;\; \xi_H \, \lambda_s \, \Delta \,. \tag{14}$$

*2.1.3. Calcium concentration* Together with the mechanical equilibrium which affects the focal adhesion formation, a calcium growth model is included to describe the evolution of calcium concentration in the cell. The governing equations include a reaction-diffusion equation representing the growth of IP3 (inositol 1,4,5- triphosphate), followed by a rate equation to determine the calcium growth [20]. The reaction-diffusion equation establishes a mechanosensitive feedback loop considering the IP3 growth which regulates the calcium concentration in the cell's cytoplasm:

$$\dot{\bar{S}} \;\; = \;\; m_s \, k \, T \, \frac{\partial^2 \bar{S}}{\partial x_i^2} - k_d \, \bar{S} + \frac{\alpha_c}{b} \, max(0, \dot{\xi}_H) - \bar{S} \, \dot{\varepsilon}(\phi) \tag{15}$$

where $\bar{S}$ is the IP3 concentration, $x_i \, (i = 1, 2)$ is the spatial coordinate in the plane and $m_s$ represents the mobility of IP3. The reaction terms involve the rate constant $k_d$ for the hydrolysis of IP3 into IP2, a non-dimensional proportionality constant $\alpha_c$ and the rate value $\dot{\xi}_H$ representing the change of the focal adhesion concentration. The strain rate of the stress fibers at an angle $\phi$ is represented by $\dot{\varepsilon}(\phi)$. For details about the growth model and the related mechanosensitive feedback loop including appropriate boundary and initial conditions, we refer to [16]. The growth of calcium depending on the available IP3 concentration follows from the rate equation:

$$\dot{C} \;\; = \;\; \lambda_f \, \frac{\bar{S}}{\bar{S}_0} \, (1 - C) - \lambda_b \, C \tag{16}$$

where $C$ represents the calcium concentration and $\lambda_f$ and $\lambda_b$ are the forward and backward rate constants, respectively.

*2.2. Staggered vs. monolithic solution approach*

The mechanical equilibrium, eq. (1), and the focal adhesion growth, eq. (13), constitute a coupled multi-physics model for the analysis of cell contractility and related stress fiber growth through focal adhesion formation. The solution of the governing equations requires to consider the influence of one solution field on the other, and vice versa. The coupling can be performed in a *staggered* or in a *monolithic* approach, depicted in Fig 2.

In a staggered approach, cf. Figure 2(a), the problem is solved in consecutive steps. The mechanical equilibrium assumes the focal adhesion formation, in terms of its high affinity integrin concentration ($\xi_H$), to be constant as obtained at the end of the previous time step $t_{n-1}$. The $\xi_H$ concentration of the current time step $t_n$ is used to evaluate the displacement field $\mathbf{u}$ of the following time step, $t_{n+1}$. Using the new displacement solution, the stretch is evaluated to update the $\xi_H$ concentration. The coupling of $\mathbf{u}$ and $\xi_H$ is done explicitly, which limits the size of the time step that can be used to ensure a stable and reliable solution.

Alternatively, the monolithic solution approach, cf. Figure 2(b), couples the governing equations (1) and (13) in a common system of equations to allow for the simultaneous solution of the unknown displacements $\mathbf{u}$ and high affinity integrin concentrations $\xi_H$. Thus, both solution fields are assumed to be varying and thereby equilibrium is established together in an iterative solution scheme. In
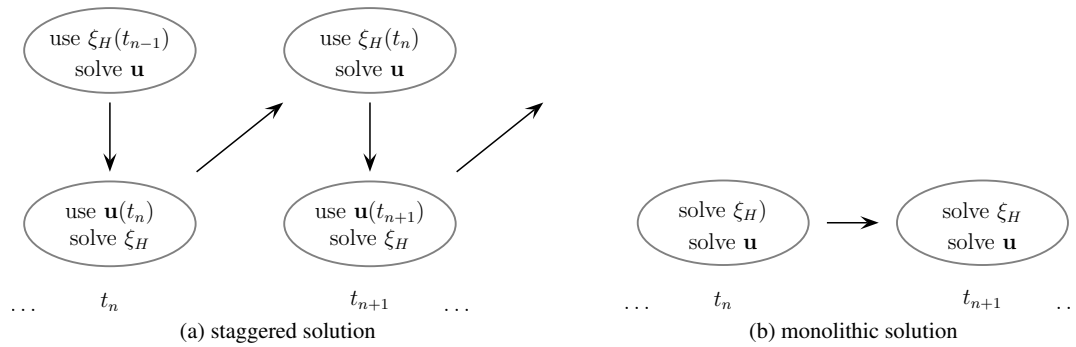
Figure 2. Solution schemes for the coupled cell contractility and focal adhesion formation.

comparison with the staggered scheme, the size of the time step used in the monolithic scheme is of minor effect on the solution quality since both solution fields are coupled implicitly and updated in a common step. In particular, the tight coupling of displacements and integrin concentrations ensures a high level of robustness of the solution process as will be demonstrated in section 5.

## 3. GEOMETRICALLY NON-LINEAR VARIATIONAL FORMULATION

*In-vitro* experiments on the contractility response of cells are commonly performed with the help of a silicon-based organic polymer substrate used as an elastic carrier material for the tested cell solution. Appropriate experiments apply any cell loading to the substrate which is subjected to large stretches. In the following variational formulation of the coupled governing equations, we account for the large displacements of in-vitro tested cells and extend the linear formulation of [16] to a geometrically non-linear formulation. To this end, we briefly introduce the non-linear elements used in the variational formulations of the considered solution schemes. A detailed representation of the underlying non-linear concepts can be found in e.g. [21].

### 3.1. Kinematics

In Figure 3, a body is depicted in an undeformed configuration at time $t = 0$, denoted with $\mathcal{B}^0$, and a deformed configuration at time $t \neq 0$, denoted with $\mathcal{B}$. In the following, we use the initial configuration $\mathcal{B}^0$ as a reference configuration in a Total-Lagrangian Formulation.
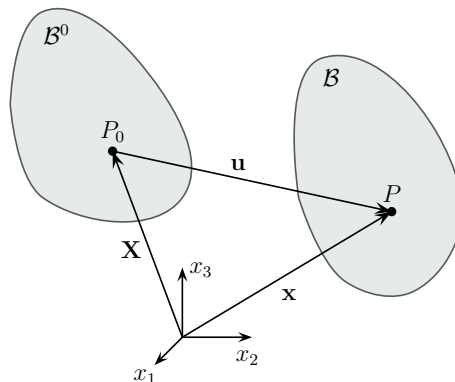


Figure 3. Undeformed reference configuration $\mathcal{B}^0$ and deformed configuration $\mathcal{B}$ of a body.

Material points of the reference configuration $\mathcal{B}^0$ are identified by a location vector $\mathbf{X}$ measured with respect to a stationary reference frame $(x_1, x_2, x_3)$ with the basis vectors

$$\mathbf{e}_i \quad = \quad \frac{\partial \mathbf{X}}{\partial x_i} \qquad\qquad i = 1, 2, 3 \,. \tag{17}$$

Material points of the current configuration $\mathcal{B}$ are identified correspondingly by a location vector $\mathbf{x}$. With the change of the configuration of the body, the displacement state $\mathbf{u}$ and the deformation gradient $\mathbf{F}$ follow as

$$\mathbf{u} \quad = \quad \mathbf{x} - \mathbf{X} \tag{18}$$

$$\mathbf{F} \quad = \quad \frac{\partial \mathbf{x}}{\partial \mathbf{X}} \,. \tag{19}$$

Using the deformation gradient (19), the Green-Lagrange strain tensor is defined conventionally as

$$\mathbf{E} \quad = \quad \frac{1}{2} \left( \mathbf{F}^T \mathbf{F} - \mathbf{I} \right) \tag{20}$$

$$E_{ij} \quad = \quad \frac{1}{2} \left( \frac{\partial u_i}{\partial X_j} + \frac{\partial u_j}{\partial X_i} + \sum_k \frac{\partial u_k}{\partial X_i} \frac{\partial u_k}{\partial X_j} \right) \qquad i, j, k = 1, 2, 3 \,. \tag{21}$$

### 3.2. Statics

The energetic conjugate stress measure to the Green-Lagrange strains are the $2^{nd}$ Piola-Kirchhoff stresses which are computed using the three-dimensional constitutive relations. A linear relation between stress and strain rates can be established with the assumption of small strains

$$\dot{\mathbf{S}} \quad = \quad \mathbb{C} : \dot{\mathbf{E}} \tag{22}$$

$$\dot{S}_{ij} \quad = \quad C_{ijkl} \, \dot{E}_{kl} \tag{23}$$

where $\mathbb{C}$ is a fourth order material tensor [21]. The $2^{nd}$ Piola-Kirchhoff stresses refer to the known reference configuration $\mathcal{B}^0$ without having a physical interpretation. The true stresses of the deformed body are the Cauchy stresses $\boldsymbol{\tau}$ which refer to the unknown current configuration $\mathcal{B}$. They are determined from the $2^{nd}$ Piola-Kirchhoff stresses by the transform

$$\boldsymbol{\tau} \quad = \quad \frac{\rho}{\rho_0} \, \mathbf{F} \, \mathbf{S} \, \mathbf{F}^T \tag{24}$$

where $\rho$ and $\rho_0$ denote the material density in the current and reference configuration, respectively.

### 3.3. Governing equations

In the following, we introduce a variational formulation on basis of the Principle of Virtual Work and derive corresponding linearized equations for an incremental iterative solution with a staggered and with a monolithic solution approach. The model considered in the analysis of the presented study, cf section 5, refers to a square domain representing the cell and the focal adhesion distribution. Symmetry of the solution domain is considered and therefore only a quarter of the domain is modeled as depicted in Figure 4. The governing equations follow a coordinate representation of a plane state of stress in which the Einstein summation convention is applied and indices take values $\{1, 2\}$.

*3.3.1. Staggered solution approach* In the staggered approach, the equations governing the mechanical equilibrium and the focal adhesion growth are considered in separate solution steps. The Total Lagrangian formulation of the virtual work of the equilibrium (1) refers all quantities to the reference configuration $\mathcal{B}^0$ :

$$\delta \mathcal{W} \quad = \quad 0 \quad = \quad b \int_{\Omega_0} S_{ij} : \delta E_{ij} \, d\Omega + \int_{\Omega_0} (\xi_H \, \bar{F}_i) \, \delta u_i \, d\Omega \tag{25}$$
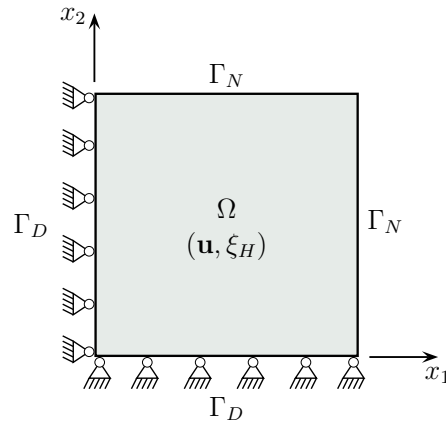
Figure 4. Solution domain $\Omega$ with symmetric Dirichlet boundary $\Gamma_D$ and Neumann boundary $\Gamma_N$, solved for the state variables $\mathbf{u}$ and $\xi_H$.

where the $2^{nd}$ Piola-Kirchhoff stress $S_{ij} = S_{ij}^a + S_{ij}^p$ represents the sum of active and passive stress in the stress fiber.

The equation (25) is non-linear and requires a stepwise incremental solution. A consistent linearization of the governing equations expresses the *unknown* instant state of a variable $\hat{a}$ at time $(t + \Delta t)$ in terms of its *known* value $a$ of the instant configuration at time $t$ and the *unknown* incremental growth $\Delta a$ from time $t$ to $t + \Delta t$. We will use this notation in the following linearization. Neglecting all higher order non-linear terms the linearized incremental equations follow as:

$$0 = \delta\mathcal{W}_{(L\Delta)} + \delta\mathcal{W}_{(N\Delta)} - \delta\mathcal{W}_{(L)} \tag{26}$$

$$\delta\mathcal{W}_{(L\Delta)} = b\int_{\Omega_0} \left(C_{ijkl}^a \Delta E_{kl}^L\right) \delta(\Delta E_{ij}^L)\, d\Omega + b\int_{\Omega_0} \left(C_{ijkl}^p \Delta E_{kl}^L\right) \delta(\Delta E_{ij}^L)\, d\Omega$$
$$+ \int_{\Omega_0} \xi_H \left(\frac{\partial(\Delta\bar{F}_i)}{\partial(\Delta u_j)}\Delta u_j\right) \delta(\Delta u_i)\, d\Omega \tag{27}$$

$$\delta\mathcal{W}_{(N\Delta)} = b\int_{\Omega_0} S_{ij}^a\, \delta(\Delta E_{ij}^N)\, d\Omega + b\int_{\Omega_0} S_{ij}^p\, \delta(\Delta E_{ij}^N)\, d\Omega \tag{28}$$

$$\delta\mathcal{W}_{(L)} = b\int_{\Omega_0} S_{ij}^a\, \delta(\Delta E_{ij}^L)\, d\Omega + b\int_{\Omega_0} S_{ij}^p\, \delta(\Delta E_{ij}^L)\, d\Omega + \int_{\Omega_0} \xi_H\, \bar{F}_i\, \delta(\Delta u_i)\, d\Omega \tag{29}$$

where the subscripts $(L\Delta)$ and $(N\Delta)$ indicate the terms to be linear and non-linear in the displacement increments $(\Delta u)$, respectively, and subscript $(L)$ denotes quantities which refer to the known instant configuration at time $t$, representing the equilibrium of the previous step. The first term of (27) represents the linearization of the active stress contribution which follows from the evaluation of the *Hill*-type growth model, eq. (2), whereas the second term represents the passive stress contribution corresponding to a linear elastic material behaviour.

*Discrete equations of the staggered solution* The domain is discretized with quadrilateral elements using bi-linear *Lagrange* functions to interpolate the unknown displacement increments:

$$\Delta\mathbf{u} = \sum_{k=1}^n N_k(x_1, x_2)\, \Delta\mathbf{U}_k = \mathbf{N}\,\Delta\mathbf{U} \tag{30}$$

$$\delta(\Delta\mathbf{u}) = \sum_{k=1}^n N_k(x_1, x_2)\, \delta(\Delta\mathbf{U}_k) = \mathbf{N}\,\delta(\Delta\mathbf{U}) \tag{31}$$

where $N_k$ represent the bi-linear shape functions assembled in a matrix $\mathbf{N}$ and $\mathbf{U}_k$ the $k^{th}$ unknown nodal degrees of freedom in the plane, assembled in a vector $\mathbf{U}$. Taking the derivatives of (30) and

(31) with respect to the global coordinates provides an interpolation rule for the incremental strain coordinates and corresponding variation which are assembled in matrices $\mathbf{B}_L$ and $\mathbf{B}_N$ to account for the linear and non-linear contributions, respectively. A detailed representation of the interpolation matrices can be found in e.g. [21]. Substitution of the discretization into the governing equations (26) and assembly ($\mathcal{A}_e$) of all elements yields:

$$\mathcal{A}_e\{\mathbf{0} \quad = \quad \delta(\Delta\mathbf{U})^T \left(\mathbf{K}_L + \mathbf{K}_N\right)\Delta\mathbf{U} - \delta(\Delta\mathbf{U})^T\mathbf{F}_{int}\} \tag{32}$$

with the element contributions:

$$\mathbf{K}_L \quad = \quad b\int_{\Omega_0} \mathbf{B}_L^T\mathbf{C}^p\,\mathbf{B}_L\,d\Omega + b\int_{\Omega_0} \mathbf{B}_L^T\mathbf{C}^a\mathbf{B}_L\,d\Omega + \int_{\Omega_0} \xi_H\mathbf{N}^T\frac{\partial\bar{\mathbf{F}}}{\partial\mathbf{U}}\mathbf{N}\,d\Omega \tag{33}$$

$$\mathbf{K}_N \quad = \quad b\int_{\Omega_0} \mathbf{B}_N^T\mathbf{S}^a\,\mathbf{B}_N\,d\Omega + b\int_{\Omega_0} \mathbf{B}_N^T\mathbf{S}^p\,\mathbf{B}_N\,d\Omega \tag{34}$$

$$\mathbf{F}_{int} \quad = \quad b\int_{\Omega_0} \mathbf{B}_L^T\hat{\mathbf{S}}^a\,d\Omega + b\int_{\Omega_0} \mathbf{B}_L^T\hat{\mathbf{S}}^p\,d\Omega + \int_{\Omega_0} \xi_H\mathbf{N}^T\bar{\mathbf{F}}\,d\Omega \tag{35}$$

where, $\hat{\mathbf{S}}^a$ and $\hat{\mathbf{S}}^p$ are the active and passive stress tensors in Voigt notation and $\bar{\mathbf{F}} = \lambda_s\,\boldsymbol{\Delta}$ denotes the interaction force contribution which results from the bond between focal adhesion and cell, and a corresponding stretch $\boldsymbol{\Delta}$, cf eq. (14), not to be confused with the deformation gradient $\mathbf{F}$, eq. (19). The last term of eq. (33) contains the linearization of the interaction force $\bar{\mathbf{F}}$ which is evaluated subject to the condition:

$$\dot{\boldsymbol{\Delta}} = \dot{\mathbf{u}} \tag{36}$$

which relates the evolution of stretch and displacement assuming a perfect bond of the integrins and the cell membrane. Using a *first order forward Euler* approach to express the unknown stretch and corresponding linearization renders the last integral term as:

$$\int_{\Omega_0} \xi_H\mathbf{N}^T\frac{\partial\bar{\mathbf{F}}}{\partial\mathbf{U}}\mathbf{N}\,d\Omega \quad = \quad \int_{\Omega_0} \xi_H\,\lambda_s\mathbf{N}^T\mathbf{N}\,d\Omega\,. \tag{37}$$

Finally, the assembled element contributions result in a linear system of equations representing the governing incremental equations of the mechanical equilibrium:

$$\left[\mathbf{K}_T\right]\left[\Delta\mathbf{U}\right] \quad = \quad \left[\mathbf{R}\right] \tag{38}$$

where $\mathbf{K}_T$ is the tangent stiffness matrix assembled from the linear and non-linear element stiffness contributions and $\mathbf{R} = \mathbf{F}_{ext} - \mathbf{F}_{int}$ is the residual at the beginning of the solution step for the unknown instant configuration at time $t + \Delta t$. After each time step the known displacement field is used to evaluate the stretch which allows the computation of the integrin ratio $\alpha$ and finally to update the higher affinity integrin concentration, cf. eq. (13).

*3.3.2. Monolithic solution approach* The monolithic solution approach solves the mechanical equilibrium and the focal adhesion growth in a common solution step. In addition to the chemo-mechanical equilibrium (25), the conservation of the total number of integrins, eq. (12), must be satisfied by the unknown high affinity integrins, which leads to a tight coupling of mechanical equilibrium and focal adhesion growth. The virtual work expression (25) is extended by a corresponding term from equation (13):

$$\delta\mathcal{W} \quad = \quad 0 \quad = \quad b\int_{\Omega_0} S_{ij}\,:\,\delta E_{ij}\,d\Omega + \int_{\Omega_0} (\xi_H\,\bar{F}_i)\,\delta u_i\,d\Omega$$

$$+ \int_{\Omega_0} \xi_H\,\delta\xi_H\,d\Omega - \int_{\Omega_0} \xi_0\frac{\alpha}{1+\alpha}\,\delta\xi_H\,d\Omega\,. \tag{39}$$

The consistent linearization of the non-linear equilibrium (39) follows the principles introduced in sub-section 3.3.1 and leads to the following contributions:

$$0 = \delta\mathcal{W}^{(u)}_{(L\Delta)} + \delta\mathcal{W}^{(u)}_{(N\Delta)} - \delta\mathcal{W}^{(u)}_{(L)} + \delta\mathcal{W}^{(\xi)}_{(L\Delta)} - \delta\mathcal{W}^{(\xi)}_{(L)} \tag{40}$$

$$\delta\mathcal{W}^{(u)}_{(L\Delta)} = b\int_{\Omega_0}\left(C^a_{ijkl}\,\Delta E^L_{kl}\right)\delta(\Delta E^L_{ij})\,d\Omega + b\int_{\Omega_0}\left(C^p_{ijkl}\,\Delta E^L_{kl}\right)\delta(\Delta E^L_{ij})\,d\Omega$$
$$+ \int_{\Omega_0}\xi_H\left(\frac{\partial(\Delta\bar{F}_i)}{\partial(\Delta u_j)}\Delta u_j\right)\delta(\Delta u_i)\,d\Omega \tag{41}$$

$$\delta\mathcal{W}^{(u)}_{(N\Delta)} = b\int_{\Omega_0}S^a_{ij}\,\delta(\Delta E^N_{ij})\,d\Omega + b\int_{\Omega_0}S^p_{ij}\,\delta(\Delta E^N_{ij})\,d\Omega \tag{42}$$

$$\delta\mathcal{W}^{(u)}_{(L)} = b\int_{\Omega_0}S^a_{ij}\,\delta(\Delta E^L_{ij})\,d\Omega + b\int_{\Omega_0}S^p_{ij}\,\delta(\Delta E^L_{ij})\,d\Omega + \int_{\Omega_0}\xi_H\,\bar{F}_i\,\delta(\Delta u_i)\,d\Omega \tag{43}$$

$$\delta\mathcal{W}^{(\xi)}_{(L\Delta)} = \int_{\Omega_0}\Delta\xi_H\,\delta(\Delta\xi_H)\,d\Omega \tag{44}$$

$$\delta\mathcal{W}^{(\xi)}_{(L)} = \int_{\Omega_0}\xi_0\frac{\alpha}{1+\alpha}\,\delta(\Delta\xi_H)\,d\Omega - \int_{\Omega_0}\xi_H\,\delta(\Delta\xi_H)\,d\Omega \tag{45}$$

where the superscripts $(u)$ and $(\xi)$ indicate the origin of the corresponding work contribution.

*Discrete equations of the monolithic solution* The unknown high affinity integrins of the governing equations are interpolated applying the same discretization that is used for the unknown displacement field

$$\xi_H = \sum_{j=1}^{n}N_j(\Delta\xi_H)_j = \hat{\mathbf{N}}\,\Delta\boldsymbol{\xi}_H \tag{46}$$

$$\delta\xi_H = \sum_{j=1}^{n}N_j\,\delta(\Delta\xi_H)_j = \hat{\mathbf{N}}\,\delta(\Delta\boldsymbol{\xi}_H) \tag{47}$$

where $\hat{\mathbf{N}}$ assembles the bi-linear Lagrange shape functions in a shape vector and $\Delta\boldsymbol{\xi}_H$ represents scalar nodal degrees of freedom. Substitution of the discretization into the governing equations (40) and assembly $(\mathcal{A}_e)$ of all elements yields:

$$\mathcal{A}_e\{\mathbf{0} = \delta(\Delta\mathbf{U})^T\left(\mathbf{K}^{uu}_L + \mathbf{K}^{uu}_N\right)\Delta\mathbf{U} + \delta(\Delta\mathbf{U})^T\mathbf{K}^{u\xi}\,\Delta\boldsymbol{\xi} \tag{48}$$

$$+\delta(\Delta\boldsymbol{\xi})^T\mathbf{K}^{\xi\xi}\,\Delta\boldsymbol{\xi} - \delta(\Delta\mathbf{U})^T\mathbf{F}^u_{int} - \delta(\Delta\boldsymbol{\xi})^T\mathbf{F}^\xi_{int}\} \tag{49}$$

with the element contributions:

$$\mathbf{K}^{uu}_L = b\int_{\Omega_0}\mathbf{B}^T_L\mathbf{C}^p\,\mathbf{B}_L\,d\Omega + b\int_{\Omega_0}\mathbf{B}^T_L\mathbf{C}^a\mathbf{B}_L\,d\Omega + \int_{\Omega_0}\xi_H\,\lambda_s\,\mathbf{N}^T\mathbf{N}\,d\Omega \tag{50}$$

$$\mathbf{K}^{uu}_N = b\int_{\Omega_0}\mathbf{B}^T_N\mathbf{S}^a\,\mathbf{B}_N\,d\Omega + b\int_{\Omega_0}\mathbf{B}^T_N\mathbf{S}^p\,\mathbf{B}_N\,d\Omega \tag{51}$$

$$\mathbf{K}^{u\xi} = \int_{\Omega_0}\mathbf{N}^T\hat{\mathbf{F}}\,\hat{\mathbf{N}}\,d\Omega \tag{52}$$

$$\mathbf{K}^{\xi\xi} = \int_{\Omega_0}\hat{\mathbf{N}}^T\hat{\mathbf{N}}\,d\Omega \tag{53}$$

$$\mathbf{F}^u_{int} = b\int_{\Omega_0}\mathbf{B}^T_L\hat{\mathbf{S}}^a\,d\Omega + b\int_{\Omega_0}\mathbf{B}^T_L\hat{\mathbf{S}}^p\,d\Omega + \int_{\Omega_0}\xi_H\mathbf{N}^T\bar{\mathbf{F}}\,d\Omega \tag{54}$$

$$\mathbf{F}^\xi_{int} = \int_{\Omega_0}\xi_0\frac{\alpha}{1+\alpha}\hat{\mathbf{N}}^T\,d\Omega - \int_{\Omega_0}\hat{\mathbf{N}}^T\hat{\mathbf{N}}\,\boldsymbol{\xi}_H\,d\Omega \tag{55}$$

in which the $(2N \times N)$-matrix $\mathbf{K}^{u\xi}$ is a coupling matrix relating the unknown high affinity integrins to the unknown displacements of the chemo-mechanical problem. Its transpose $\mathbf{K}^{\xi u} = \mathbf{0}$, leads to a non-symmetric system of equations. The system matrices assembled from (50) to (53) and the corresponding system vectors assembled from (54) and (55) provide the linearized system of equations of the monolithic solution approach:

$$
\begin{bmatrix} \mathbf{K}^{uu} & \mathbf{K}^{u\xi} \\ \mathbf{0} & \mathbf{K}^{\xi\xi} \end{bmatrix} \begin{bmatrix} \Delta\mathbf{U} \\ \Delta\boldsymbol{\xi} \end{bmatrix} = \begin{bmatrix} \mathbf{R}^u \\ \mathbf{R}^\xi \end{bmatrix} \tag{56}
$$

where the incremental displacement field and the incremental high affinity integrins are solved in the same step. The established monolithic coupling is based on a one-way dependence of the high affinity integrins on the stretch of the focal adhesion induced bond.

*3.3.3. Feedback loop mechanism* The feedback loop mechanism of sub-section 2.1.3 relates the calcium growth to the stress fiber formation in the cell and requires an independent solution of the reaction-diffusion equation (15) with the variational representation:

$$
\int_\Omega \dot{\bar{S}} \, (\delta\bar{S}) \, d\Omega = -D \int_\Omega \frac{\partial \bar{S}}{\partial x_i} \frac{\partial(\delta\bar{S})}{\partial x_i} \, d\Omega + R \tag{57}
$$
$$
\text{with} \quad R = -k_d \int_\Omega \bar{S} \, (\delta\bar{S}) \, d\Omega - \dot{\varepsilon} \int_\Omega \bar{S} \, (\delta\bar{S}) \, d\Omega + \frac{\alpha_c}{b} \, max(0, \dot{\xi}_H) \int_\Omega \delta\bar{S} \, d\Omega
$$

in which the variation of the IP3 concentration $(\delta\bar{S})$ is chosen as appropriate test function, and $D = (m_s \, k \, T)$ is the diffusion coefficient while $R$ denotes the reaction terms. The analysis domain considers *no-flux* conditions along the Neumann boundary $\Gamma_N$ and an initial domain IP3 concentration $s_0$ including the Dirichlet boundary $\Gamma_D$ where $s_0$ is the reference IP3 concentration, cf Table I:

$$
-D \frac{\partial \bar{S}}{\partial x_i} \, n_i = 0 \quad \forall \, x_i \in \Gamma_N \tag{58}
$$
$$
\bar{S} = s_0 \quad \forall \, x_i \in \Omega \supset \Gamma_D \,. \tag{59}
$$

The change of the IP3 concentration with time on the left-hand side of eq. (57) is resolved in terms of a first order forward Euler approach:

$$
\dot{\bar{S}} = \frac{\bar{S}(t + \Delta t) - \bar{S}(t)}{\Delta t} := \frac{\bar{S} - \bar{S}^t}{\Delta t} \tag{60}
$$

in which $\Delta t$ is the time step increment and $\bar{S}^t$ is the known primal field variable of the previous time step.

The spatial discretization follows the bi-linear approach introduced in the sub-section 3.3.2 using the interpolation approach (46) and (47) with the shape functions $\hat{\mathbf{N}}$ and their corresponding spatial derivatives $\hat{\mathbf{N}}_{,x}$ resulting in the governing algebraic equations:

$$
\mathcal{A}_e \{ \mathbf{0} = \delta\bar{\mathbf{S}}^T \, (\mathbf{M}_{\bar{S}} + \mathbf{K}_{\bar{S}}) \, \bar{\mathbf{S}} + \delta\bar{\mathbf{S}}^T \, (\mathbf{F}_t + \mathbf{F}_{\xi_H}) \} \tag{61}
$$

with the element contributions:

$$
\mathbf{M}_{\bar{S}} = \int_\Omega \left( \frac{1}{\Delta t} + k_d + \dot{\varepsilon} \right) \hat{\mathbf{N}} \, \hat{\mathbf{N}}^T \, d\Omega \tag{62}
$$

$$
\mathbf{K}_{\bar{S}} = \int_\Omega D \, \hat{\mathbf{N}}_{,x} \, \hat{\mathbf{N}}_{,x}^T \, d\Omega \tag{63}
$$

$$
\mathbf{F}_t = \int_\Omega \frac{\bar{S}^t}{\Delta t} \hat{\mathbf{N}} \, d\Omega \tag{64}
$$

$$
\mathbf{F}_{\xi_H} = \int_\Omega \left( \frac{\alpha_c}{b} \, max(0, \dot{\xi}_H) \right) \hat{\mathbf{N}} \, d\Omega \,. \tag{65}
$$

The governing linear system of equations is solved in each time step to provide the current IP3 concentration $\bar{\mathbf{S}}$ which is used to predict the calcium production that initiates the focal adhesion growth. The calcium growth, eq. (16), is solved by an embedded Runge-Kutta scheme, a single-step approach which approximates the solution considering two Runge-Kutta estimates of different order to allow for a control of the truncation error with adaptive step-size [22].

## 4. ALGORITHMIC ASPECTS

The governing algebraic equations of section 3.3 reveal the essential differences between the staggered and the monolithic approaches, and how the coupling of the chemo-mechanical equations is established. The different schemes have direct effect on the structure and algebraic properties of the governing system of equations, and thus on the single solution steps including stability and robustness of the solution. In the following section, we illustrate the different nature of the schemes from an algorithmic perspective and highlight some of the solution properties which are further addressed in the example section.

---

**Data:** model geometry and material parameter values as provided in Table I [16]
**Result:** nodal displacements $\mathbf{u}$ and high affinity integrin concentrations $\boldsymbol{\xi}_H$ and corresponding
increments at time $t = t_{end}$, assembled in a common solution vector $\mathbf{V} := [\mathbf{U}; \boldsymbol{\xi}_H]$ and
$\Delta\mathbf{V} := [\Delta\mathbf{U}; \Delta\boldsymbol{\xi}_H]$, respectively.

*% model setup and initialization*
setupAnalysisModel();
$t = 0$;

*% incremental time step loop*
**while** $t < t_{end}$ **do**

    *% mechanosensitive feedback update: evaluate IP3 concentration using an embedded*
    *% Runge-Kutta method , eq. (15)*
    $\bar{S} = \text{IP3Production}(m_s, k, T, \alpha_c, k_d, b, \dot{\xi}_H, \dot{\varepsilon}(\Phi))$;

    *% evaluate calcium concentration, eq. (16)*
    $C = \text{calciumConcentration}(\bar{S}, \bar{S}_0, \lambda_f, \lambda_b)$;

    *% evaluate stress fiber concentration, eq. (4)*
    $\eta = \text{stressFiberConcentration}(\lambda_f, \lambda_b, C, \kappa, \phi)$;

    *% Newton-Raphson iteration until stopping criteria is satisfied*
    **while** $\delta^i > \varepsilon_r \, \delta^t$ **do**

        *% solution of the governing system of equations (56), quantities refer to time $t + \Delta t$*
        $\mathbf{K}^{i-1} \, \Delta\mathbf{V}^i = \mathbf{F}_{ext}^{i-1} - \mathbf{F}_{int}^{i-1}$;

        *% solution update in iteration $i$ of time step $t + \Delta t$*
        $\mathbf{V}^i = \mathbf{V}^{i-1} - \Delta\mathbf{V}^i$;

        *% update of the convergence parameters*
        $\delta^i = \max(\ \text{abs}(\mathbf{U}^i - \mathbf{U}^{i-1})\ )$;
        $\delta^t = \max(\ \text{abs}(\mathbf{U}^i - \mathbf{U}^t)\ )$;

        *% increment iteration step*
        $i = i + 1$;
    **end**
    *% increment time step*
    $t = t + \Delta t$;
**end**

**Algorithm 1:** Monolithic solution scheme for the analysis of the chemo-mechanical cell response.

---

The algorithmic structure of the monolithic and staggered solution schemes is depicted in Algorithms 1 and 2, respectively. Both schemes start with entering a time step loop and the computation of the stress fiber concentration $\eta$, used to update the isometric stress $\sigma_0$ and thus the active stress $\sigma^a$ in the mechanical equilibrium. The stress fiber concentration $\eta$ requires an update of the calcium concentration in the cell and thus the evaluation of the current IP3 concentration, eq. (15), which is solved by an embedded Runge-Kutta-method [22] establishing the feedback loop between the focal adhesion formation and the stress fiber generation.

---

**Data:** model geometry and material parameter values as provided in Table I [16]
**Result:** nodal displacements $\mathbf{u}$ and high affinity integrin concentrations $\boldsymbol{\xi}_H$ and corresponding
       increments at time $t = t_{end}$.

*% model setup and initialization*
setupAnalysisModel();
$t = 0$;

*% incremental time step loop*
**while** $t < t_{end}$ **do**

    *% mechanosensitive feedback update: evaluate IP3 concentration using an embedded*
    *% Runge-Kutta method , eq. (15)*
    $\bar{S} = \text{IP3Production}(m_s, k, T, \alpha_c, k_d, b, \dot{\xi}_H, \dot{\varepsilon}(\Phi))$;

    *% evaluate calcium concentration, eq. (16)*
    $C = \text{calciumConcentration}(\bar{S}, \bar{S}_0, \lambda_f, \lambda_b)$;

    *% evaluate stress fiber concentration, eq. (4)*
    $\eta = \text{stressFiberConcentration}(\lambda_f, \lambda_b, C, \kappa, \phi)$;

    *% Newton-Raphson iteration until stopping criteria is satisfied*
    **while** $\delta^i > \varepsilon_r \, \delta^t$ **do**

        *% solution of the governing system of equations (38), quantities refer to time $t + \Delta t$*
        $\mathbf{K}^{i-1} \, \Delta \mathbf{U}^i = \mathbf{F}_{ext}^{i-1} - \mathbf{F}_{int}^{i-1}$;

        *% solution update in iteration $i$ of time step $t + \Delta t$*
        $\mathbf{U}^i = \mathbf{U}^{i-1} - \Delta \mathbf{U}^i$;

        *% update of the convergence parameters*
        $\delta^i = \max(\text{abs}(\mathbf{U}^i - \mathbf{U}^{i-1}))$;
        $\delta^t = \max(\text{abs}(\mathbf{U}^i - \mathbf{U}^t))$;

        *% increment iteration step*
        $i = i + 1$;
    **end**

    *% update high affinity integrins using equations (11) and (13)*
    $\xi_H = f(\xi_0, \Delta(\mathbf{U}))$

    *% increment time step*
    $t = t + \Delta t$;
**end**

**Algorithm 2:** Staggered solution scheme for the analysis of the chemo-mechanical cell response.

---

The monolithic scheme solves the unknown displacement field and high affinity integrins using an incremental iterative Newton-Raphson method. In each iteration step, the tangent matrix and inner forces are updated with the total displacements to account for the non-linear cell deformation. In contrast, the staggered scheme solves only for the unknown displacement field within the Newton-Raphson iteration using the high affinity integrin concentrations of the previous time step. The integrins of the current step are updated in a follower step on basis of the current displacements.

Both algorithms use a convergence criteria which is exclusively based on the computed total displacements which is a natural choice for the staggered scheme but also a reasonable choice for the monolithic scheme since the high affinity integrins are directly dependent on the stretch and therefore dependent on the displacement field. An error constant $\varepsilon_r$ of order $10^{-3}$ appeared sufficient in all computations to ensure robustness and reliability of the non-linear analysis.

## 5. NUMERICAL EXPERIMENTS

In the following, we study the interaction of the mechanical response of the cell and the focal adhesion growth using the bio-chemo-mechanical cell model. In particular, we analyze the solution properties of the staggered and monolithic solution approaches. We consider performance aspects for the different solution methods with respect to stability and numerical reliability. To this end, we consider a model refinement in space and time. Next, we study the robustness of the two solution methods for different model configurations considering variation of dominant model parameters. Finally, we consider a substrate supported cell model subject to cyclic loading and analyze the stress fiber reorientation over time.

| parameter | symbol | unit | value |
|---|---|---|---|
| Passive elastic modulus | $E$ | kPa | 0.08 |
| Poisson's ratio of cell | $\nu$ | | 0.3 |
| Tensile strength of stress fibers | $\sigma_{max}$ | kPa | 20 |
| Maximum stretch | $\Delta_{max}$ | m | $1.30e-7$ |
| Focal adhesion bond stiffness | $\lambda_s$ | N/m | $1.50e-5$ |
| Boltzmann constant | $k_b$ | $\text{m}^2 \text{ kg s}^{-2} \text{ K}^{-1}$ | $1.38e-23$ |
| Temperature | $T$ | K | 310 |
| Difference between reference chemical potentials of high and low affinity integrins | $\Delta\mu$ | $\text{m}^2 \text{ kg s}^{-2}$ | $5 \, k_b \, T$ |
| Reference integrin concentration | $\xi_0$ | integrins/m$^2$ | $5.0e+15$ |
| IP3 mobility constant | $m_s$ | s/kg | $1.0e+10$ |
| IP3 diffusion proportionality constant | $\alpha_s$ | | 10 |
| IP3 de-phosphorylation rate constant | $k_d$ | s$^{-1}$ | $5.0e-4$ |
| Reference IP3 concentration | $s_0$ | molecules/m$^3$ | $1.0e+21$ |
| Forward rate constant of Calcium release | $\lambda_f$ | s$^{-1}$ | 1.0 |
| Backward rate constant of Calcium release | $\lambda_b$ | s$^{-1}$ | 0.5 |

Table I. Applied model parameters following [23].

### 5.1. Convergence properties

We study the analysis domain depicted in Figure 4 with the model properties provided in Table I. The parameters were chosen according to a model setup proposed in DESHPANDE ET AL. [23] to mimic the experimental results of TAN ET AL. [24]. In the following we denote this choice of parameters as *base configuration*. Symmetry boundary conditions were applied along the left and lower boundary and zero traction boundary conditions were applied along the right and upper domain boundary. The model is loaded by an initial IP3 concentration $s_0$ which triggers the growth of the feedback loop coupled active stress and focal adhesion.

The focal adhesion growth is expected to form towards the boundary of the cell. Accordingly, the initial finite element mesh was refined adaptively towards the domain boundary and three different meshes were considered, cf. Figure 5. It is noted that the same discretization was used for both sub-models, the elasticity problem and the focal adhesion growth problem. The total time span of the simulation, needed to account for a steady-state solution, varies for the different model parameters between $200s$ and $4000s$. The time step size was chosen in the interval $[0.5s, 4.0s]$.
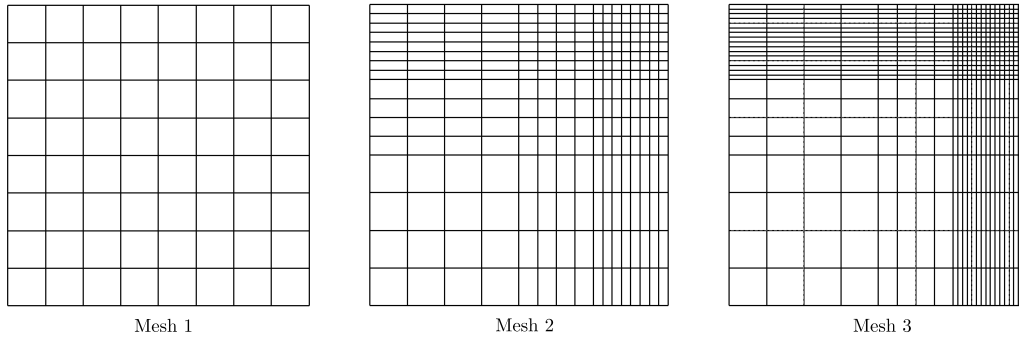
Figure 5. Finite element meshes with 64 elements (mesh 1), 256 elements (mesh 2) and 576 elements (mesh 3).
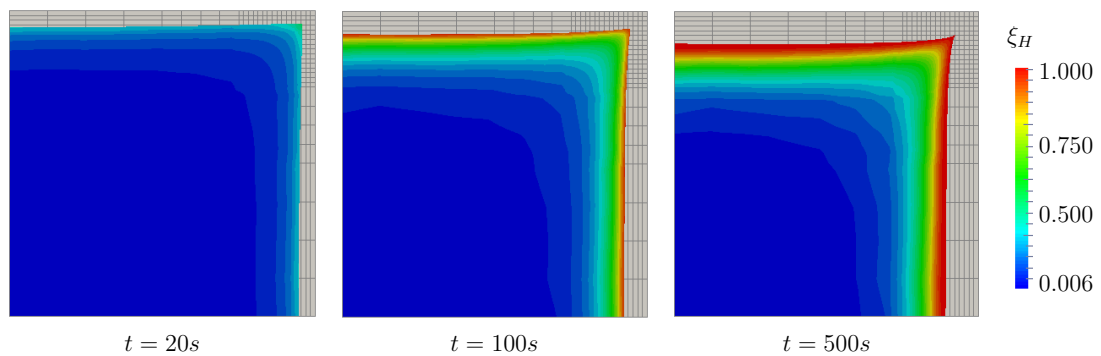


Figure 6. Focal adhesion growth on the deformed cell at different time steps (scale factor = 14).

The expected focal adhesion growth is evident from the results shown in Figure 6. It represents the temporal evolution of the focal adhesion formation on the deformed cell at different time steps of the parameter base configuration.
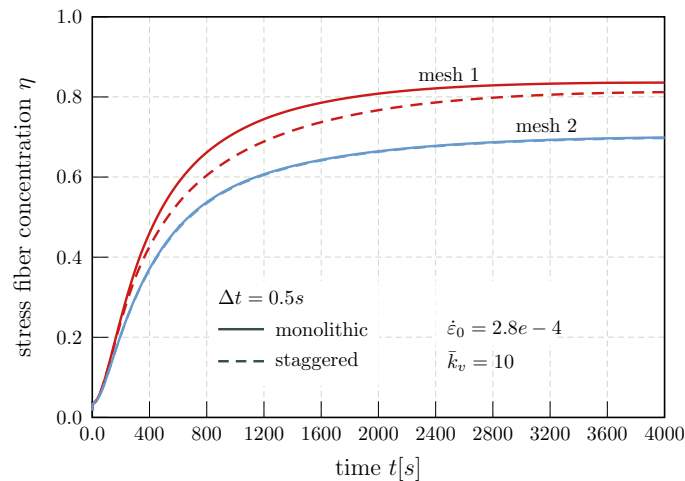


Figure 7. Mesh refinement for focal adhesion growth - base configuration.

The stress fiber growth for the base configuration is depicted in Figure 7, indicating convergence for both solution schemes for chosen time step $\Delta t = 0.5\,s$. The refined mesh (mesh 2) shows virtually identical results for the staggered and monolithic solution methods. Even for the unrefined mesh (mesh

1), the results of the two methods have a relative difference of less than 3%. The good match of the staggered and monolithic solution scheme was observed throughout all computations which led to the same steady-state solution, irrespective of the value of the chosen time step size.

The need for mesh refinement is evident with the results depicted in Figures 7 and 9. A linear convergence rate was observed for all problems, showing a model error of $\approx 2\%$ for the finest discretization using corresponding estimates for the exact steady state solution based on a Richardson extrapolation [25]. The convergence of the stress fiber concentration at the mid-point of the domain boundary is given in Figure 8.
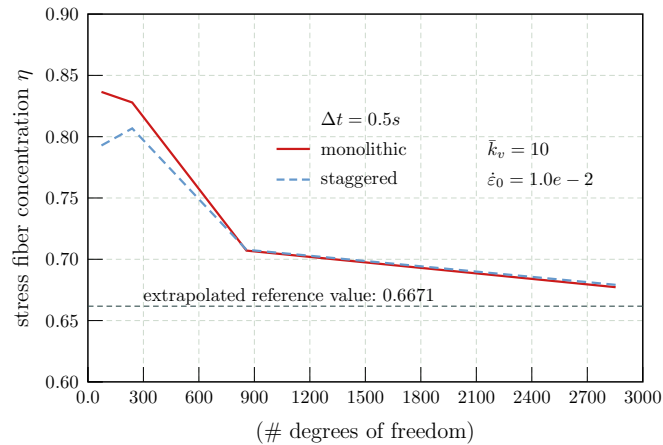


Figure 8. Convergence of the stress fiber concentration with mesh refinement.

In Figure 9(a), the stress fiber growth is shown for a modified Hill constant $\bar{k}_v$, reduced from $\bar{k}_v = 10$ to $\bar{k}_v = 1$, with the effect that the steady-state solution is obtained already after one-third of the simulation time of the base configuration, cf. Fig. 7. An increase of the time step size from $0.5s$ to $2s$ has no influence with respect to convergence behaviour and the value of the steady-state solution. The dimensionless Hill constant $\bar{k}_v$ represents a velocity coefficient which relates the stress growth in the stress fibers to the strain rate. A raise of $\bar{k}_v$ has the direct effect of an increasing growth rate of the active stress $\sigma^{(a)}$ which is used in the dissociation part of the stress fiber growth. An increase of $\sigma^{(a)}$ reduces the dissociation of stress fibers and promotes the association part of the stress fiber concentration rate, thus lowering the overall growth rate. Conversely, the stress fiber growth activates faster when $\bar{k}_v$ is reduced.



(a) modified Hill coefficient $\bar{k}_v$

(b) modified strain rate $\dot{\varepsilon}_0$
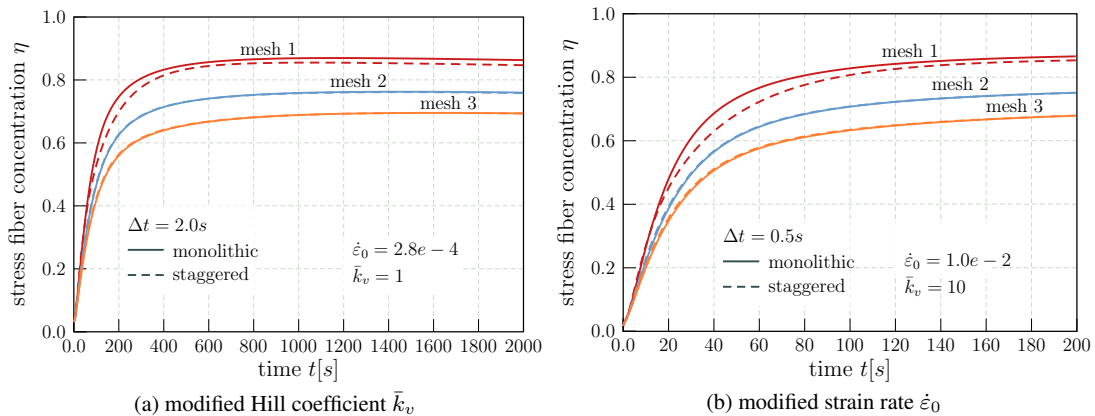
Figure 9. Comparison of staggered vs. monolithic schemes for different mesh refinements.

The increase of the strain rate from $\dot{\varepsilon}_0 = 2.8e - 4$ to $\dot{\varepsilon}_0 = 0.01$ accelerates the growth of the stress fiber concentration even more as shown in Figure 9(b). Both modifications of the base configuration lead to an increased stress fiber concentration of about $8\%$, which indicates a reduction of the stress fiber association due to an increased active stress level.



(a) modified Hill coefficient $\bar{k}_v$        (b) modified strain rate $\dot{\varepsilon}_0$
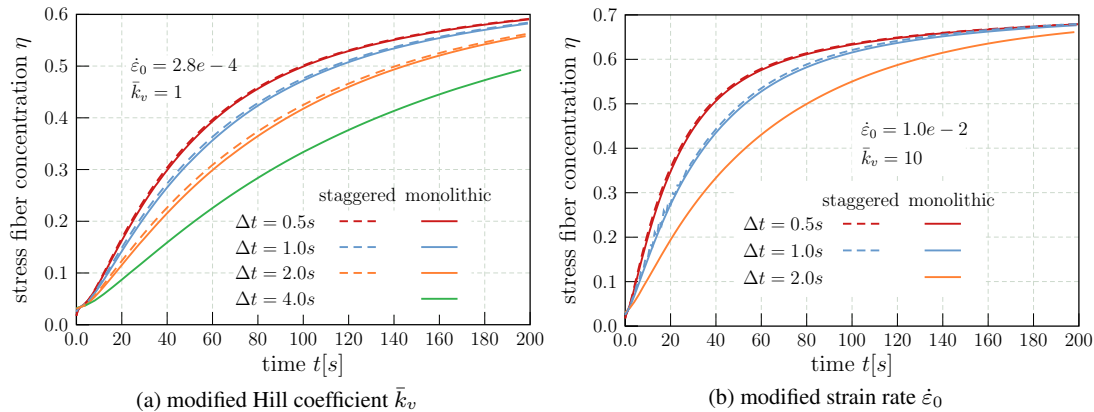
Figure 10. Comparison of staggered vs. monolithic schemes for different time step increments, finest mesh.
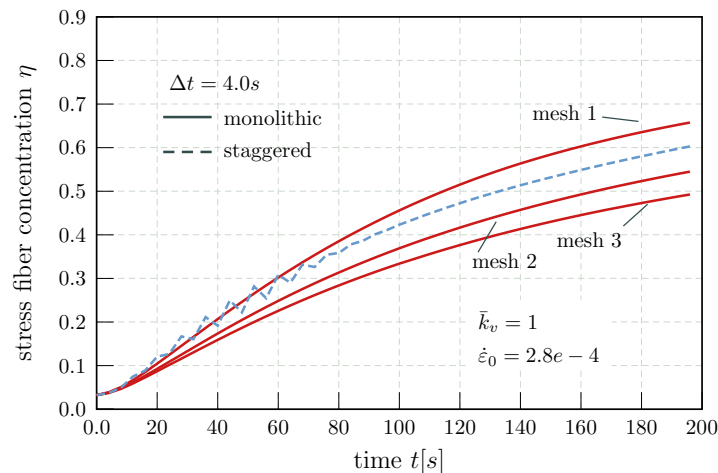


Figure 11. Oscillatory behavior of the staggered solution scheme.

Next, we consider the influence of the time step size on robustness, reliability and numerical effort of the analysis. Time steps $\Delta t$ of $0.5s, 1s, 2s$ and $4s$ were taken and a robust solution was obtained for the base configuration. Even for a time step $\Delta t = 6s$ convergence was achieved with both schemes but only for the base configuration whereas in all other parameter configurations only the monolithic scheme succeeded. The models with modified Hill-coefficient and strain rate, depicted in Figures 10(a) and 10(b), respectively, showed a different behavior. For a Hill-coefficient $\bar{k}_v = 1.0$ the staggered scheme failed to compute a steady-state solution for $\Delta t = 4s$. The failure occurred during the Newton-Raphson iteration which we used for the solution of the non-linear equilibrium equations. In the case of a increased strain rate to $\dot{\varepsilon}_0 = 0.01$, the staggered scheme failed already for $\Delta t = 2s$.

In sum, the robustness of the staggered scheme was weaker than that of the monolithic scheme and showed some discretization sensitivity in terms of an oscillatory behaviour already at a time step size $\Delta t = 1s$, cf. Figure 10(b), and aggravated for larger time step sizes as depicted in Figure 11. This behavior was not observed in any computation with the monolithic scheme, irrespective of the chosen time step size and mesh density.

The higher robustness of the monolithic scheme compared to the staggered scheme is clearly visible from the comparison of Figure 12 which shows virtually no difference in the focal adhesion growth for the staggered solution scheme using a time step of $\Delta t = 0.5s$ and for the monolithic approach with a time step $\Delta t = 4s$.



<div align="center">

$\xi_H$

$1.00e + 00$

$5.03e - 01$

$6.69e - 03$

</div>

(a) staggered solution, $\Delta t = 0.5s$         (b) monolithic solution, $\Delta t = 4.0s$
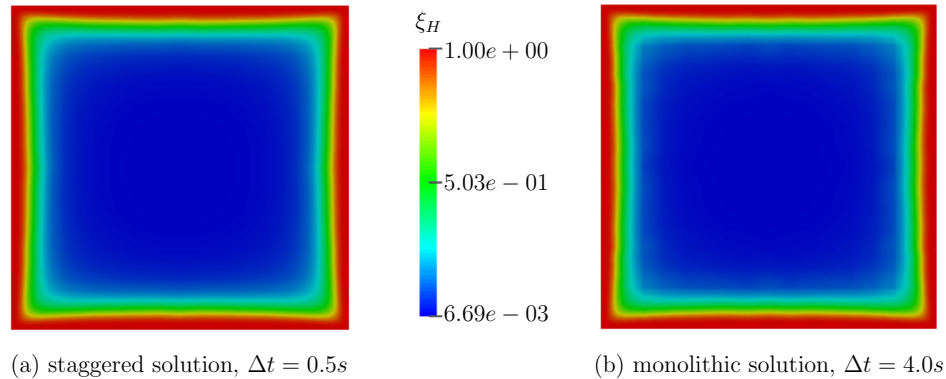
Figure 12. Focal adhesion growth for staggered and monolithic methods at $t = 2000s$.

## 5.2. Cyclic loading

Next, the model was tested for a cyclic loading of a substrate supported cell to mimic *in-vitro* experiments subject to external load patterns. Cells form a bond with the substrate through focal adhesion, which results in stress transfer from the substrate to the cell. We assume a perfect bond between substrate and the cell. Following the experiments reported in [26], the substrate was loaded with a constant uni-axial cyclic loading according to the load pattern shown in Figure 13, where $d = 3s$, $1/f = 110s$ and $\varepsilon_0 = 0.32$. The evaluated stress was considered in the mechanical equilibrium, eq. (1), including the effect of the substrate with a stiffness of $20kPa$.



(a) Substrate supported cell         (b) Cyclic loading pattern
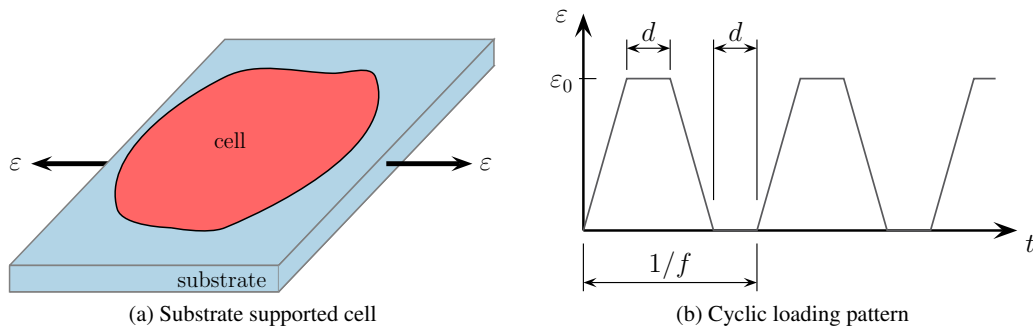
Figure 13. Cyclic loading of a substrate supported cell.

The importance of this test lies in the observation that during the unloading phase, the stress fiber concentration along the direction perpendicular to the loading direction is higher than in the loading direction. This behavior is visible from Figure 14 where the $\phi = 90°$ curves cut the $\phi = 0°$ curves at the level of $\eta \approx 0.2$ which was simulated by both solution schemes but at different conditions. In Figure 14, the stress fiber concentration for the steady state response is depicted after $1500s$ in the direction of loading ($\phi = 0°$) and perpendicular to it ($\phi = 90°$). The chosen time steps of $\Delta t = 4s$ for the monolithic scheme and $\Delta t = 1s$ for the staggered scheme reveal differences in amplitude and phase. The large time step size of the monolithic scheme exceeds the core length ($d = 3s$) of the trapezoidal loading function which leads to a constant phase shift. For smaller time steps $\Delta t \leq 2s$ the response curves are congruent.
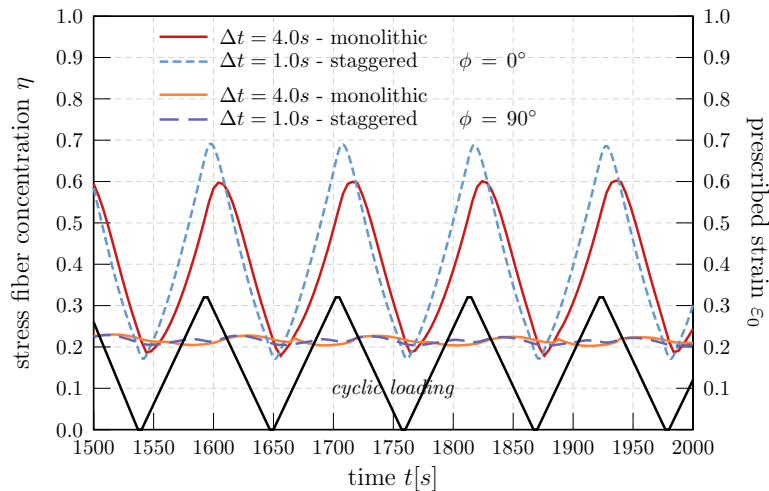
Figure 14. Cyclic loading response with load function (in black).

The key conclusion of this test is of a qualitative nature and in accordance with observations from *in-vitro* testing [26]. For the cyclic loading we observed that the temporal variation of the stress fiber concentration is affected, i.e. the stress fiber concentration varies with the fiber angles. As the cyclic loading progresses, the stress fiber concentration at $\phi = 0°$ dissociates during the unloading phase more than that in the perpendicular direction. In contrast, we observed that during the beginning of the cyclic loading, the stress fiber concentration is higher along the direction of loading than in the perpendicular direction. This observation is visualized in the circular histograms of Figure 15 which reveal a fiber re-orientation over the simulation time towards the direction perpendicular to the loading direction, representing strain avoidance.

The computation of the stress fiber concentration at each angle and time step is computationally intensive but can be eased by using higher time step increments as is possible with the monolithic solver. The qualitative observation of a stress fiber re-orientation behaviour obtained with the monolithic solver and a large time step size matches the experimental observations very well.



(a) monolithic, $\Delta t = 4s$         (b) staggered, $\Delta t = 1s$
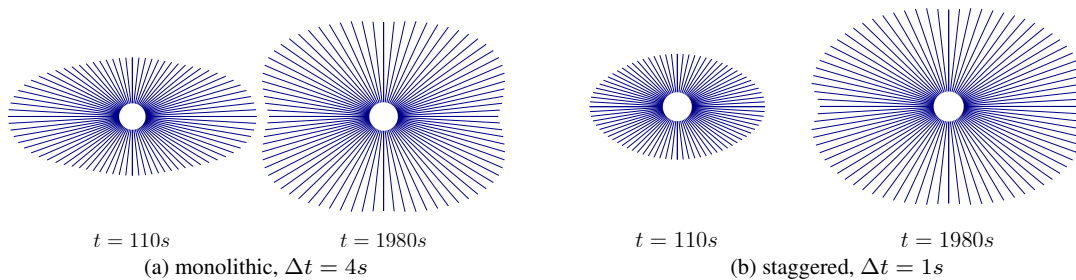
Figure 15. Circular histograms – qualitative comparison of stress fiber growth subjected to cyclic loading along the horizontal direction ($\longleftrightarrow$).

### 5.3. Performance aspects

It is worth noting that the system of equations of the monolithic scheme, eq. (56), has a factor $1.5$ more degrees of freedom than the system of equations of the staggered scheme, eq. (38), which is solved in two independent steps considering matrices of dimensions $2N$ and $N$. Furthermore, the monolithic scheme cannot exploit symmetry properties during the solution process. As a consequence of the different scales involved in the solution of the mechanical response and the focal adhesion concentration, the system matrices are extremely ill-conditioned. Despite a pre-conditioning prior to

the solution, a severe numerical sensitivity remains which is reflected in the large number of iterations needed by the Newton-Raphson method to obtain equilibrium in each step, cf. Figure 16. We used a direct solver for both methods to account for sufficient stability. The higher numerical effort needed to factorize the non-symmetric system matrix of the monolithic scheme compared to the smaller and symmetric system matrix of the staggered scheme was easily compensated by the significantly larger time step used in the monolithic scheme. Regarding the numerical complexity of the two solution schemes, the monolithic method saves a factor $> 3$ which pays off for the considered time spans. We observed in all computations the monolithic scheme to be more stable at a slightly fewer number of iterations and applicable to all tested temporal and spatial discretizations.
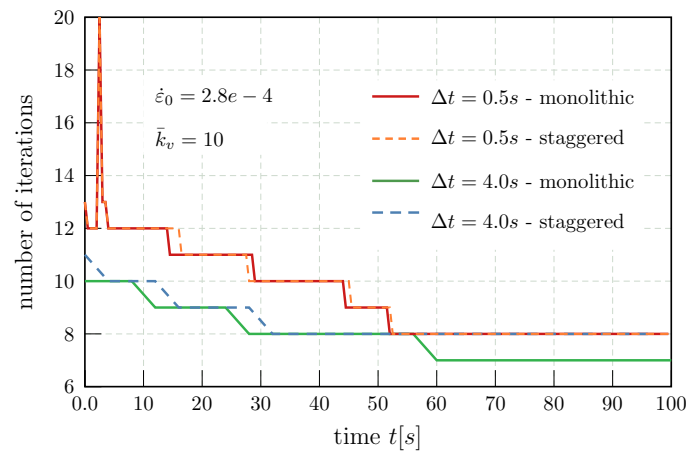


Figure 16. Total number of iterations per time step.

## 6. SUMMARY, CONCLUSIONS AND OUTLOOK

We have explored the properties of solution schemes for a bio-chemo-mechanical model which represents the multi-physical behavior of cells including elastic deformation, focal adhesion growth and stress fiber re-orientation due to cyclic loading. We derived two variationally consistent continuum formulations, coupling the different physics in terms of monolithic and staggered numerical solution schemes. The mechanical sub-model considers large displacements and a Hill-type growth model for active stress and a linear elastic passive stress model represents the internal forces of the balance equations. The chemical sub-model represents the potentials of low and high affinity integrins which satisfy a thermo-dynamical equilibrium by conversion of low and high affinity concentrations considering elastic energy and bond energy due to tensile forces applied to the bearing cell substrate. Finally, the model was completed by a feedback loop which relates the focal adhesion growth and the stress fiber formation through an update of the calcium concentration in the cell. Based on the variational formulation, we derived the governing algebraic equations of the monolithic and the staggered solution schemes and provided an algorithmic description of the two solution procedures. Furthermore, we provided the variational and discrete reaction-diffusion model of the feedback-loop mechanism which is solved in each analysis step.

With the two derived solution schemes, we studied the growth of the stress fiber concentration in the cell over time and tested the numerical performance of the two methods. To this end, we considered a continuous model refinement in space and time which revealed the need for adaptive refinement and a good match of the two methods for small time step increments. Despite a broad agreement of the different solution schemes with regard to accuracy and convergence behavior, we observed an overall higher robustness and reliability for the monolithic approach. In particular, with increasing time step size, the staggered approach repeatedly failed to provide a steady-state solution and showed a distinct mesh sensitivity which was observed already at smaller time steps. Both numerical models ameliorate

an ill-conditioned system of equations by a pre-conditioning. Still, the number of iterations needed to regain equilibrium in each time step is high and suggests to revisit this issue in future implementations. Next, we studied the variation of strain rate and the Hill constant, both having influence on the speed of convergence to a steady-state solution but at different rates. All tests showed a widely congruent result for a large time step monolithic solution in comparison with a small time step staggered solution, the latter showing reliability only for small time steps. In sum, the monolithic scheme has the potential to save a significant number of analysis steps due to the possibility to apply a substantially larger time step. An average saving of $\approx 70\%$ was observed with regard to the number of solution steps, with ensuing drastic effects on the total computational effort. It is the higher stability and robustness of the monolithic scheme compared to the staggered approach which constitutes the most notable advantage, more so than the gain in computational times.

Finally we studied stress fiber re-orientation of a substrate supported cell subjected to uni-axial cyclic loading to mimic experiments performed *in-vitro*. They confirmed the efficiency of the monolithic approach in the context of computationally demanding time-history simulations in cell mechanics.

## REFERENCES

1. Mih JD, Marinkovic A, Liu F, Sharif AS, Tschumperlin DJ. Matrix stiffness reverses the effect of actomyosin tension on cell proliferation. *Journal of Cell Science* 2012; **125**(24):5974–5983, doi:10.1242/jcs.108886.
2. Chan CE, Odde DJ. Traction dynamics of filopodia on compliant substrates. *Science* 2008; **322**(5908):1687–1691, doi:10.1126/science.1163595.
3. Hochmuth RM. Micropipette aspiration of living cells. *Journal of Biomechanics* 2000; **33**(1):15–22, doi:10.1016/S0021-9290(99)00175-X.
4. Cui Y, Hameed FM, Yang B, Lee K, Pan CQ, Park S, Sheetz M. Cyclic stretching of soft substrates induces spreading and growth. *Nature Communications* 2015; **6**:6333, doi:10.1038/ncomms7333.
5. Kaunas R, Usami S, Chien S. Regulation of stretch-induced JNK activation by stress fiber orientation. *Cellular Signalling* 2006; **18**(11):1924–1931, doi:10.1016/j.cellsig.2006.02.008.
6. Tondon A, Hsu HJ, Kaunas R. Dependence of cyclic stretch-induced stress fiber reorientation on stretch waveform. *Journal of Biomechanics* 2012; **45**(5):728–735, doi:10.1016/j.jbiomech.2011.11.012.
7. Ingber DE. Tensegrity I. Cell structure and hierarchical systems biology. *Journal of Cell Science* 2003; **116**(Pt 7):1157–1173.
8. Satcher RL, Dewey CF. Theoretical estimates of mechanical properties of the endothelial cell cytoskeleton. *Biophysical Journal* 1996; **71**(1):109–118, doi:10.1016/S0006-3495(96)79206-8.
9. Deshpande VS. Analysis and interpretation of stress fiber organization in cells subject to cyclic stretch. *Journal of Biomechanical Engineering* 2008; **130**(3):031 009, doi:10.1115/1.2907745.
10. Vernerey FJ, Farsad M. A constrained mixture approach to mechano-sensing and force generation in contractile cells. *Journal of the Mechanical Behavior of Biomedical Materials* 2011; **4**(8):1683–1699, doi:10.1016/j.jmbbm.2011.05.022.
11. Obbink-Huizer C, Oomens CWJ, Loerakker S, Foolen J, Bouten CVC, Baaijens FPT. Computational model predicts cell orientation in response to a range of mechanical stimuli. *Biomechanics and Modeling in Mechanobiology* 2014; **13**(1):227–236, doi:10.1007/s10237-013-0501-4.
12. Hübner B, Walhorn E, Dinkler D. A monolithic approach to fluid-structure interaction using space-time finite elements. *Computer Methods in Applied Mechanics and Engineering* 2004; **193**(23-26):2087–2104, doi:10.1016/j.cma.2004.01.024.
13. Michler C, Hulshoff S, van Brummelen E, de Borst R. A monolithic approach to fluid–structure interaction. *Computers & Fluids* 2004; **33**(5-6):839–848, doi:10.1016/j.compfluid.2003.06.006.
14. Küttler U, Gee M, Förster C, Comerford A, Wall WA. Coupling strategies for biomedical fluid-structure interaction problems. *International Journal for Numerical Methods in Biomedical Engineering* 2010; **26**(3-4):305–321, doi:10.1002/cnm.1281.
15. Markert B. *Weak or Strong: On Coupled Problems in Continuum Mechanics*. No. II-20 in Report / Universität Stuttgart, Institut für Mechanik (Bauwesen), Lehrstuhl II, Institut für Mechanik (Bauwesen), Lehrstuhl II: Stuttgart, 2010. OCLC: 699868505.
16. Keshavanarayana P, Ruess M, de Borst R. A feedback-loop extended stress fiber growth model with focal adhesion formation. *International Journal of Solids and Structures* 2017; **128**:160–173, doi:10.1016/j.ijsolstr.2017.08.023.
17. Küttler U, Gee M, Förster C, Comerford A, Wall WA. Coupling strategies for biomedical fluid-structure interaction problems. *International Journal for Numerical Methods in Biomedical Engineering* 2010; **26**(3-4):305–321, doi:10.1002/cnm.1281.
18. Hill AV. The heat of shortening and the dynamic constants of muscle. *Proceedings of the Royal Society of London B: Biological Sciences* 1938; **126**(843):136–195, doi:10.1098/rspb.1938.0050.
19. Deshpande VS, Mrksich M, Mcmeeking RM, Evans A. A bio-mechanical model for coupling cell contractility with focal adhesion formation. *Journal of the Mechanics and Physics of Solids* 2008; **56**(4):1484–1510, doi:10.1016/j.jmps.2007.08.006.
20. Pathak A, McMeeking RM, Evans AG, Deshpande VS. An analysis of the cooperative mechano-sensitive feedback between intracellular signaling, focal adhesion development, and stress fiber contractility. *Journal of Applied Mechanics* 2011; **78**(4):041 001, doi:10.1115/1.4003705.

21. Borst R, A Crisfield M, Remmers J, Verhoosel C. *Nonlinear Finite Element Analysis of Solids and Structures*. 2nd edn., Wiley: Chichester, 2012.
22. Press W, Teukolsky S, Vetterling W, Flannery B. *Numerical Recipes - The Art of Scientific Computing*. 3 edn., Cambridge University Press, 2007.
23. Deshpande VS, McMeeking RM, Evans AG. A bio-chemo-mechanical model for cell contractility. *Proceedings of the National Academy of Sciences* 2006; **103**(38):14 015–14 020, doi:10.1073/pnas.0605837103.
24. Tan JL, Tien J, Pirone DM, Gray DS, Bhadriraju K, Chen CS. Cells lying on a bed of microneedles: An approach to isolate mechanical force. *Proceedings of the National Academy of Sciences* 2003; **100**(4):1484–1489.
25. Soroushian A, Wriggers P, Farjoodi J. Asymptotic upper bounds for the errors of Richardson extrapolation with practical application in approximate computations. *International Journal for Numerical Methods in Engineering* 2009; **80**:565–595.
26. Faust U, Hampe N, Rubner W, Kirchgeßner N, Safran S, Hoffmann B, Merkel R. Cyclic Stress at mHz Frequencies Aligns Fibroblasts in Direction of Zero Strain. *PLoS ONE* 2011; **6**(12):e28 963, doi:10.1371/journal.pone.0028963.